The Astrophysical Journal, 896:139 (11pp), 2020 June 20 https://doi.org/10.3847/1538-4357/ab910f

Photospheric Polarization Signatures from Long Gamma-Ray Burst Simulations

Tyler Parsotan[1], Diego López-Cámara[2], and Davide Lazzati[1]
[1] Department of Physics, Oregon State University, 301 Weniger Hall, Corvallis, OR 97331, USA
[2] CONACyT—Instituto de Astronomía, Universidad Nacional Autónoma de México, A. P. 70-264 04510 CDMX, Mexico
Received 2020 March 25; revised 2020 May 2; accepted 2020 May 5; published 2020 June 22

Abstract

A comprehensive understanding of gamma-ray bursts (GRBs) has been elusive due to the variety of questions surrounding the radiation mechanism at play in these events. Polarization measurements of GRBs can heavily constrain the relevant radiation mechanisms and the structure of the GRB jet; however, there is a limited number of theoretical predictions that observed GRB polarizations can be compared against. Here, we conduct radiative transfer calculations of a set of two-dimensional relativistic hydrodynamic long GRB (LGRB) jet simulations, of a constant and a variable jet, using the Monte Carlo Radiation Transport (MCRaT) code. MCRaT has been enhanced by the inclusion of polarization; it has been first verified by reproducing a variety of results in the literature and then used to obtain the time-integrated and time-resolved polarization degrees and angles of the synthetic LGRBs. While the obtained time-integrated polarization degrees ($\lesssim$1%) are consistent with the constraints from the POLAR experiment, they are lower than other theoretical studies due to the lack of strong gradients in the model jet profiles that we use. The time-resolved results suggests that GRBs with wide jets observed on axis will have small polarization degrees ($\lesssim$2%) and constant polarization angles, during the brightest portion of the light curve. GRBs observed off-axis will have larger polarization degrees and polarization angles that change with the temporal structure of radiating shells in the outflow. We then place our results in the context of GRB prompt emission models and future LEAP and POLAR-2 GRB polarimetry detections.

Unified Astronomy Thesaurus concepts: Gamma-ray bursts (629); Hydrodynamics (1963); Radiative transfer simulations (1967)

1. Introduction

Gamma-ray bursts (GRBs) have been detected since the late 1960s as a relatively short pulse of gamma-ray photons (Klebesadel et al. 1973). These transient events have been categorized based on their duration. Events that last $\lesssim$2 s are short GRBs and are associated with the merger of compact objects (Abbott et al. 2017; Goldstein et al. 2017; Lazzati et al. 2018) while events that last for $\gtrsim$2 s are denoted long GRBs (LGRBs) and are associated with core-collapse supernovae (Bloom et al. 1999; MacFadyen et al. 2001; Hjorth et al. 2003). Regardless of the type of GRB that is observed, the physical mechanism that produces the high energy X-ray and γ-ray photons that are observed during the first few seconds of these events, known as the prompt emission, is still under investigation.

There are currently two major competing theories: the synchrotron model (SM) (Rees & Mészáros 1994; Zhang & Yan 2010) and the photospheric model (Rees & Mészáros 2005; Pe'er et al. 2006; Lazzati et al. 2009; Beloborodov 2010). The optically thin SM describes shells of material, which are launched with varying speeds by a central engine, colliding with one another far from the central engine. These collisions produce nonthermal radiation which is able to escape the jet if the opacity $\tau < 1$. This model is able to account for general characteristics of GRBs such as variability and nonthermal spectra, but is in tension with observational relationships such as the Amati, Yonetoku, and Golenetskii correlations (Golenetskii et al. 1983; Amati et al. 2002; Yonetoku et al. 2004; Zhang & Yan 2010). Although Mochkovitch & Nava (2015) showed that the internal shock model can satisfy the Amati relation under certain conditions, there have been other subcategories of synchrotron models developed in an attempt to rectify these discrepancies. These models consider the effects of both globally ordered and random magnetic fields (Toma et al. 2009; Zhang & Yan 2010).

On the other hand, the photospheric model follows photons that have been produced deep in the jet. These photons interact with the matter in the jet until the jet becomes transparent to the radiation. Unlike the SM, this model is able to reproduce most of the observational relationships (Lazzati et al. 2013; López-Cámara et al. 2014). Subphotospheric dissipation events (Chhotray & Lazzati 2015) and the idea of the photospheric region, in which the photosphere is a volume of space in which photons can still be upscattered by sparse interactions with matter in the jet (Parsotan & Lazzati 2018; Parsotan et al. 2018; Ito et al. 2015; Pe'er 2008; Beloborodov 2010; Ito et al. 2019), contribute to the nonthermal nature of the spectra in the photospheric model. Although this model is able to reproduce general characteristics of GRBs, it is not able to fully account for the relatively large amount of low energy photons that are observed in GRB spectra.

The shortcomings of each model have placed them on relatively equal footing; however, polarization measurements of the prompt emission can help break this degeneracy. While there have been a number of polarization measurements made by a variety of instruments, the results have been largely inconclusive due to the difficulty of conducting such an observation with high precision. From the past decade, the largest linear polarization measurement reported was 98% $\pm$ 33% from GRB 041219A (Kalemci et al. 2007) and the smallest was 27% $\pm$ 11% from GRB 100826A in a time-resolved analysis (Yonetoku et al. 2011), where the reported errors are 1σ (also see Gill et al. 2019 for a comprehensive list of detected GRB polarization measurements). These measurements and many others are time integrated in order

to get as much signal as is possible, however the uncertainties are still very large. These relatively high polarizations are typically interpreted under the assumption that only synchrotron radiation can produce such high polarizations (Lyutikov et al. 2003; Waxman 2003; Burgess et al. 2019). A number of studies have shown that GRB jets with ordered magnetic fields can produce high polarizations ranging between 20%–70% (see, e.g., Toma et al. 2009; Deng et al. 2016; Lan & Dai 2020, and Gill et al. 2019), while jets with random magnetic fields produce smaller polarizations. Photospheric emission was originally thought to only produce very small polarizations, however it has been shown that this model can produce a polarization up to ∼40% if the jet has significant structure within $\delta\theta \sim \Gamma^{-1}$, where Γ is the bulk Lorentz factor of the jet (Ito et al. 2014; Lundman et al. 2014, 2018), although this configuration may not occur in GRBs. Structure in the jet refers to gradients in the jet profile and/or anisotropy in the outflow of photons (which is related to the expanding outflow) (Lundman et al. 2014). If the source of soft photons in the photospheric model is due to synchrotron emission then the detected polarization can increase up to ∼50% (Lundman et al. 2018).

Building on the polarimetry technology used to acquire past measurements, the POLAR experiment (Produit et al. 2018) recently reported time-integrated linear polarizations for five GRBs and had enough statistics to conduct a time-resolved polarization analysis for one of the GRBs, GRB 170114A (Zhang et al. 2019). Their analysis showed that the GRBs had relatively small upper limits for their time-integrated linear polarizations, with the largest upper limit being 68% and the smallest upper limit being 28%; typically they find that the linear polarizations are $\lesssim$10%. The authors claim that although GRB 170114A had a small time-integrated linear polarization, the time-resolved portions of the GRB show relatively high polarization ($\gtrsim$10%) with a continually changing polarization angle. In acquiring these results, Zhang et al. (2019) make a number of assumptions about the physics of the GRB polarization, such as assuming that polarization degree is constant throughout a GRB and that polarization angle can change in time.

The authors interpret the changing polarization angle to be in strain with the photospheric model. Following this analysis, Burgess et al. (2019) analyzed GRB 170114A by combining information from Fermi, which also observed the GRB. They find similar results in that the SM seems to describe the GRB well despite the other weakness associated with the SM model. There is ambiguity, however, since the low linear polarization degree of GRB 170114A is easily attainable in the photospheric model. As a result, Burgess et al. (2019) call for more theoretical modeling and predictions of time-resolved polarization signatures that will inform future analysis.

There have been no prior analyses of time-integrated or time-resolved polarization angles or polarization degrees under the photospheric model using the realistic profile of a GRB jet. In this work we focus on the photospheric model and show that it is able to account for a changing polarization angle and variable polarization degrees. We use the Monte Carlo Radiation Transfer (MCRaT) code[3] to provide time-integrated polarization predictions and the first time-resolved analysis of LGRB simulations using the photospheric model. In Section 2 we describe the methods we use to conduct mock observations of our synthetic LGRBs and outline how polarization is handled in MCRaT. Finally, in Sections 3 and 4, we present the results and discuss the implications to GRB polarimetry missions and understanding the radiation mechanism in GRBs.

[3] The MCRaT code is open source and is available to download at https://github.com/lazzati-astro/MCRaT/.

2. Methods

There are numerous works that have explored polarization in the energy regime applicable to GRBs. These works have focused primarily on the Stokes parameters formalism (see, e.g., McMaster 1961; Depaola 2003; Krawczynski 2011; Ito et al. 2014; Lundman et al. 2014). Here, we describe how we conduct mock observations of the polarization degree and polarization angle, and then we describe the implementation of polarization in MCRaT and show that it is able to reproduce the results of Depaola (2003), Krawczynski (2011), and Lundman et al. (2014). For more in depth discussions of the Stokes parameters we refer the reader to the aforementioned references. Finally, we outline how we determine equal time of arrival surfaces within the hydrodynamic simulations used in this work.

2.1. Mock Observations of Polarization

We produce light curves and spectra in the same manner outlined in Parsotan & Lazzati (2018) and Parsotan et al. (2018) by collecting photons within a given viewing angle and binning them in time and energy. Here, we outline how we calculate the detected polarization degree, the polarization angle and their respective errors.

The Stokes parameters are a vector, $S = (I, Q, U, V)$ that holds information about the polarization of electromagnetic radiation. I is the intensity of the electromagnetic radiation, Q and U describe the orientation of the polarization ellipse, and V describes the ratio of the principal axis of the polarization ellipse (Rybicki & Lightman 1979). We follow the convention set by McMaster (1961) and Lundman et al. (2014) where $Q = +1$ is oriented with the y-axis of the Stokes plane and $Q = -1$ is oriented with the x-axis of the Stokes plane. The $+U$ axis is rotated 45° clockwise with respect to the $+Q$ axis and the $-U$ axis is rotated 45° clockwise with respect to the $-Q$ axis. Furthermore, we normalize the Stokes parameters such that $I = 1$ at all times giving us $s = (1, Q/I, U/I, V/I) = (1, q, u, v)$. In our simulations, we only consider linear polarization, which means that we ignore any contribution by v. This is appropriate since we assume that electron spins, which directly affect v, are isotropically distributed.

The polarization degree, Π, represents the average polarization of the detected photons (Rybicki & Lightman 1979). From the stokes parameters Π is calculated as

$$\Pi = \sqrt{\left(\frac{Q}{I}\right)^2 + \left(\frac{U}{I}\right)^2 + \left(\frac{V}{I}\right)^2} = \sqrt{q^2 + u^2}, \quad (1)$$

where the second portion of the equation takes the normalization by I into account and ignores v since we do not consider circular polarization. Since the photons in MCRaT are weighted to increase computational efficiency (one photon packet in MCRaT represents some number of real photons in the relativistic outflow), we cannot simply add each photon's detected Stokes parameters to calculate q and u; instead, we have to take the photons' weight, w, into consideration by averaging the detected photons' Stokes parameters (see Parsotan et al. (2018) for a

discussion of the weight). Thus, we calculate q and u as

$$q = \frac{\sum w_i q_i}{\sum w_i} \quad u = \frac{\sum w_i u_i}{\sum w_i}. \tag{2}$$

The error in the polarization degree, σ_Π, is given by Kislat et al. (2015) as

$$\sigma_\Pi \approx \sqrt{\frac{2 - \Pi^2 \mu^2}{(N-1)\mu^2}}, \tag{3}$$

where N is the number of photons that were detected and μ is the modulation factor. For a perfect detector $\mu = 1$, which is what we assume in this work. Additionally, the formulas acquired by Kislat et al. (2015), which we use in this work, slightly underestimate the MCRaT error bars since they do not consider variances in photon weights. Following the analysis presented in their appendix, we multiply each error bar by $\sqrt{\langle w^2 \rangle / \langle w \rangle^2}$ to account for this factor, where the angled brackets denote averages.

The polarization angle, χ, represents the net direction of the electric field vector once all the detected photons have been summed over (Kislat et al. 2015). χ, the angle between the $+q$ axis and the electric field vector, measured clockwise toward the $+u$ axis of the Stokes plane, is given by Kislat et al. (2015) as

$$\chi = \frac{1}{2} \arctan\left(\frac{u}{q}\right). \tag{4}$$

The error in the polarization angle, as given by Kislat et al. (2015), is

$$\sigma_\chi \approx \frac{1}{\Pi \mu \sqrt{2(N-1)}}. \tag{5}$$

For the simulations analyzed in this work, where we assume an axisymmetric geometry, χ should be aligned with the positive or negative Stokes Q values due to the sum of the U parameters adding to zero (Lundman et al. 2014). We verified that the number of photons used in this work are high enough that $\sum u \approx 0$. Additionally, χ has π symmetry so we plot it between $-90°$ and $+90°$.

2.2. Polarization in the MCRaT Code

In MCRaT all photons are initialized to have no polarization; thus, we set $s = (1, 0, 0, 0)$ similar to Lundman et al. (2014). Each photon becomes 100% polarized from the very first scattering that it undergoes, which does not bias our results. As mentioned before, we only consider linear polarization which means that we ignore any contribution by v.

In order to deal with polarization, we follow the prescription given by Lundman et al. (2014). We Lorentz boost the photons' four momenta from the lab frame to the fluid frame, then from the fluid frame to the electron rest frame. In the electron frame we conduct our scattering using the full Klein–Nishina (KN) cross section and then scatter the Stokes parameters using Fano's Matrix. Afterwards, we deboost the photons from the electron rest frame and the fluid rest frame back to the lab frame.

In the lab frame, the Stokes plane is oriented such that the $+Q$ axis is pointing in the $-\hat{\phi}$ direction and the $-Q$ axis is pointing in the $-\hat{\theta}$ direction. The $+U$ axis is rotated 45° clockwise with respect to the $+Q$ axis and the $-U$ axis is rotated 45° clockwise with respect to the $-Q$ axis. χ is measured clockwise from the $+Q$ axis toward the $+U$ axis. $\hat{\phi}$ and $\hat{\theta}$ are the orthonormal azimuthal and polar unit vectors in a spherical coordinate system where the radial unit vector is parallel to the photon's momentum vector. This setup is a natural outcome of using the definitions from Lundman et al. (2014).

Each boost to another reference frame entails rotating the Stokes plane using the Muller rotation matrix (McMaster 1961) given by

$$\boldsymbol{M}[\phi] = \begin{pmatrix} 1 & 0 & 0 & 0 \\ 0 & \cos 2\phi & -\sin 2\phi & 0 \\ 0 & \sin 2\phi & \cos 2\phi & 0 \\ 0 & 0 & 0 & 1 \end{pmatrix}, \tag{6}$$

where the angle of rotation, ϕ, corresponds to the rotation that orients the y-axis of the Stokes plane perpendicular to the photon three momentum and the velocity vector of the frame that the photon will be boosted into. The equation for ϕ is given in Appendix B of Lundman et al. (2014). After each boost, we rotate the Stokes plane again to ensure that the y-axis of the Stokes plane is perpendicular to the plane formed by the reference frame's z-axis and the photon's three momentum.

We use the KN cross section to determine if the photon scatters. The photons gets scattered if $\xi \leqslant \sigma_{\rm KN}/\sigma_{\rm T}$, where ξ is a random uniformly distributed number between 0 and 1, $\sigma_{\rm KN}$ is the KN cross section given by Rybicki & Lightman (1979), and $\sigma_{\rm T}$ is the Thomson cross section. If $\xi \leqslant \sigma_{\rm KN}/\sigma_{\rm T}$ then we sample the differential KN cross section to determine the angles, $\theta_{\rm sc}$ and $\phi_{\rm sc}$, that the photon will be scattered into. The differential cross section given by Lundman et al. (2014) is

$$\frac{d\sigma_{\rm KN}}{d\Omega}(\theta_{\rm sc}, \phi_{\rm sc}) = \frac{r_0^2}{2}\left(\frac{\epsilon}{\epsilon_0}\right)^2 \times \left\{\frac{\epsilon_0}{\epsilon} + \frac{\epsilon}{\epsilon_0} - \sin^2\theta_{\rm sc}(1 - q\cos 2\phi_{\rm sc} + u \sin 2\phi_{\rm sc})\right\}, \tag{7}$$

where r_0 is the classical electron radius, ϵ_0 is the incoming photon energy scaled by the electron rest mass, and $\epsilon = \epsilon_0/(1 + \epsilon_0[1 - \cos\theta_{\rm sc}])$ is the scattered photons energy. The outgoing photon's $\theta_{\rm sc}$ is acquired by rejection sampling the differential cross section integrated over $\phi_{\rm sc}$ following the method outlined by Mathews (2013) for maximum efficiency. We acquire $\phi_{\rm sc}$ by choosing a random uniformly distributed value between $[0, 2\pi]$ when $q = u = 0$, otherwise we apply a rejection sampling method to the differential KN cross section. The case of $q = u = 0$ removes the KN cross section's dependence on $\phi_{\rm sc}$, which allows us to choose a value between $[0, 2\pi]$.

Depaola (2003) presents a method of sampling the KN azimuthal distribution, however they use a KN cross section that is in a different form than the one that is employed above. Thus, we outline our method of sampling Equation (7) to acquire $\phi_{\rm sc}$ when the incoming photon is polarized. The azimuthal angle that gives the maximum of the KN differential cross section, $\phi_{\rm m}$, can be solved as

$$\phi_{\rm m} = \frac{1}{2}\left|\arctan\left(\frac{-u}{q}\right)\right|. \tag{8}$$

We then plug ϕ_m and the previously acquired θ_{sc} into the KN differential cross section to get the normalization for the rejection sampling method, $\frac{d\sigma_{KN}}{d\Omega}(\theta_{sc}, \phi_m)$. We proceed as follows:

(1) draw a random number ξ uniformly distributed between 0 and 1;
(2) draw a random ϕ_{sc} uniformly distributed between 0 and 2π;
(3) calculate $\frac{d\sigma_{KN}}{d\Omega}(\theta_{sc}, \phi_{sc})$;
(4) determine if $\xi \leqslant \left[\frac{d\sigma_{KN}}{d\Omega}(\theta_{sc}, \phi_{sc})\right]\left[\frac{d\sigma_{KN}}{d\Omega}(\theta_{sc}, \phi_m)\right]^{-1}$;
(5) if the above condition is met, accept the value of ϕ_{sc}, otherwise repeat the sampling.

Once the scattering is completed, we conduct the scattering of the Stokes parameters. First, we use the Muller matrix to rotate the Stokes plane such that the Stokes plane's y-axis is perpendicular to the plane formed by the incoming and outgoing photon three momenta (McMaster 1961; Lundman et al. 2014). Then, we use Fano's matrix, $(T[\theta_{sc}, \epsilon_0, \epsilon]$; McMaster 1961) to determine the resulting polarization, $\tilde{s} = T[\theta_{sc}, \epsilon_0, \epsilon]s$. Fano's matrix is

$$T[\theta_{sc}, \epsilon_0, \epsilon] = \begin{pmatrix} 1 + \cos^2\theta_{sc} + (\epsilon_0 - \epsilon)(1 - \cos\theta_{sc}) & \sin^2\theta_{sc} & 0 \\ \sin^2\theta_{sc} & 1 + \cos^2\theta_{sc} & 0 \\ 0 & 0 & 2\cos\theta_{sc} \end{pmatrix}, \quad (9)$$

where, similar to Krawczynski (2011), we have excluded the factors in front since they cancel out when we normalize the scattered Stokes parameters by I as mentioned above. We have also excluded the fourth row and column of the matrix since we only consider linear polarization.

We reproduce Depaola's (2003) result, as shown in Figure A1, which verifies the sampling algorithm of the differential KN cross section. Additionally, reproducing Krawczynski's (2011) results, in Figure A2, tests the Lorentz transform portion of MCRaT.

In order to test the code globally, we reproduce the results of Lundman et al. (2014). To do so, we imposed the analytic jet structure provided by Lundman et al. (2014) on the same simulation frames that we will use in Section 3. This is similar to Lazzati (2016) simulating a variety of outflows by imposing an analytic solution onto hydrodynamic simulation files. The domain of this simulation is 2.5×10^{13} cm along the direction of the jet and 5×10^{12} cm along the x-axis. We used $\sim 6 \times 10^5$ photons to conduct our code validation for a wide structured jet with $\theta_j = 0.1$ radians ($\sim 5.^\circ 7$), $\Gamma_0 = 100$, and $L = 3 \times 10^{50}$ erg s^{-1}. This is the same case exhibited in the wide jet from Lundman et al. (2014) with the exception of the value of L that we use, which was chosen to maximize the number of photons that reached the photosphere before they approached the edge of the domain of the hydrodynamic simulation. There are two major differences between the simulation conducted by Lundman et al. (2014) and the MCRaT simulation: (1) MCRaT uses the full KN cross section to determine if photons scatter while the Lundman et al. (2014) simulation uses the Thomson cross section; (2) the photons in MCRaT are not permitted to immediately escape to infinity if the randomly drawn optical depth is small enough, while photons in the Lundman et al. (2014) simulation are allowed to do so.

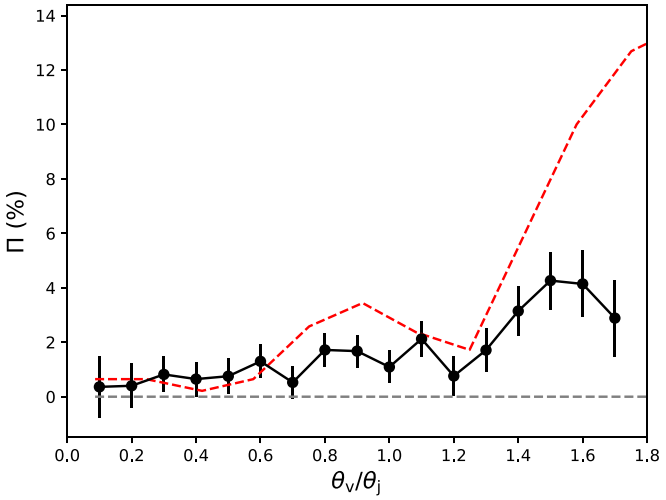

Figure 1. A comparison between the polarization acquired by Lundman et al. (2014) for a structured jet with $\theta_j = 0.1$ radians $\Gamma_0 = 100$ and $L = 3 \times 10^{50}$ erg s^{-1}, shown by the red dashed line, and the MCRaT acquired polarization shown by the black points with 1σ error bars. The dashed gray line denotes $\Pi = 0\%$ for reference. We find agreement until $\theta_v/\theta_j \approx 1.6$ ($\theta_v \approx 9^\circ$) where the MCRaT photons are no longer decoupled from the flow by the time they reach the edge of the simulation domain.

In Figure 1 we show the results of our validation. The polarization acquired by Lundman et al. (2014) is shown as the red dotted line, the black points with 1σ error bars show the polarization acquired by MCRaT, and the gray dotted line shows $\Pi = 0\%$ for reference. In addition to finding that the Stokes u parameter vanishes ($\sum u \approx 0$, see Section 2.1), which is expected for an axis-symmetric jet (Ito et al. 2014; Lundman et al. 2014), we find that MCRaT is able to recover Lundman et al.'s (2014) polarization profile relatively well. We are also able to recover the change in the sign of the Stokes Q parameter at $\theta_v/\theta_j \sim 1.2$ that Lundman et al. (2014) find in their results. The MCRaT result is slightly lower than the polarization acquired by Lundman et al. (2014) due to the fact that the analytic jet profile is mapped onto a discretized grid; this has the effect of decreasing the gradients in the jet profile that would contribute to a larger polarization. Furthermore, the Lundman et al. (2014) polarization profile contains a minimum of 200 photons in each angle bin, while the results of the MCRaT validation contain at least $\sim$10,000 photons in each angle bin, increasing the general precision of the MCRaT results.

For $\theta_v/\theta_j \gtrsim 1.6$ ($\theta_v \approx 9^\circ$) the MCRaT polarization begins to decrease again, coming into strain with what is expected. This is due to the fact that the simulation files that we impose the analytic jet equations onto have a finite domain. Even when the photons reach the edge of the domain (2.5×10^{13} cm) at $\theta_v \gtrsim 9^\circ$, they have not fully decoupled from the photosphere (which would be located at $r \sim 1 \times 10^{14}$ cm (Lundman et al. 2014)), thus decreasing the detected polarization.

2.3. Equal Time of Arrival Surfaces

In order to relate the structure of the jet in the GRB simulations to the time-dependent observables produced by MCRaT (such as the time-resolved polarization), we need to calculate the location that photons would be emitting along the observer's line of sight (LOS) for a given time in the light curve, t_{detect}. We follow the derivation for Parsotan & Lazzati's (2018) Equation (1). The time in which a photon would be

emitted from the jet, t_j, can be calculated as

$$t_j = t_{\rm detect} - t_{\rm real}, \tag{10}$$

where $t_{\rm real}$ is the real time acquired from the hydrodynamic simulation. The radius, r_j, at which a photon is emitted by the jet is

$$r_j = t_j c, \tag{11}$$

where c is the speed of light. The equal time of arrival surface (Beloborodov 2011; Pe'er & Ryde 2011; Deng & Zhang 2014) is then constructed by drawing a line tangent to the circle that passes through r_j and the observer viewing angle, $\theta_{\rm v}$

3. Results

In this work, we ran MCRaT on two different FLASH 2D special relativistic hydrodynamic (RHD) simulations which both launched a jet into a 16TI progenitor star with a density profile provided by Woosley & Heger (2006). The first simulation which we call the *16TI* simulation, has a jet injection radius of 1×10^9 cm, an initial Lorentz factor of 5, an opening angle of 10°, an internal over rest-mass energy ratio, $\eta = 80$, and the engine was active for 100 s (Lazzati et al. 2013). The domain of this simulation is 2.5×10^{13} cm along the direction of the jet. The second simulation, which we denote the *40sp_down* simulation, has a jet that was injected with similar initial conditions as the *16TI* jet with the exception of the jet being pulsed. The *40sp_down* simulation jet was on for 40 half second pulses, each followed by another half second of quiescence. The luminosity of each pulse was decreased by 5% with respect to the first pulse (López-Cámara et al. 2014). The domain of the *40sp_down* simulation is 2.56×10^{12} cm along the jet axis. These simulations were previously analyzed by Parsotan & Lazzati (2018) and Parsotan et al. (2018) where they focus on various spectral properties and the synthetic light curves. In this paper we focus on the time-integrated polarization and the time-resolved polarization properties of each simulated GRB.

We ran the MCRaT code during the time in which the central engine of each model was active in order to investigate the effects of the varying central engine on the radiation. The number of photons injected into each simulation was $\sim 1.9 \times 10^7$ for the *16TI* simulation and $\sim 1.4 \times 10^6$ for the *40sp_down* simulation. The order of magnitude difference was necessary to maintain a reasonable computation time for the *40sp_down* simulation. This is a direct result of the jet in the *40sp_down* simulation moving at $\Gamma \sim 10$ which is an order of magnitude smaller than the *16TI* simulation.

3.1. Time-integrated Polarization

Figure 2 shows the time-integrated polarization degrees, Π, angles, χ, and peak luminosity of the light curve, $L_{\rm pk}$, as a function of observer viewing angles of the synthetic GRBs. These results are acquired by integrating over the time that the jet is active. Here, we plot Π in blue, the light curve peak luminosity, $L_{\rm pk}$, in black, and χ in purple for the *16TI* simulation, in Figure 2(a), and the *40sp_down* simulation, in Figure 2(b). $L_{\rm pk}$ is the peak of the synthetic light curve when the light curve is binned into 1 s time bins, analogous to the manner in which it is used in the Yonetoku relationship. In general, we find that Π is negatively correlated to $L_{\rm pk}$, with Spearman's rank coefficients $r_s = -0.6$[4] and $r_s = -0.27$ for the *16TI* and *40sp_down* simulations, respectively. Additionally, Π is positively correlated to $\theta_{\rm v}$, where $r_s = 0.65$ and $r_s = 0.19$ for the *40sp_down* and *16TI* simulation, respectively. The direct relationship between Π and $\theta_{\rm v}$ is easy to see in Figure 2(b) for the *40sp_down* simulation, however, it becomes more complicated in the *16TI* simulation. This is due to the fact that we see a turnover in the polarization in the *16TI* simulation at $\theta_{\rm v} = 8°$, which is consistent with our verification results in Figure 1. The photons at these larger angles are not fully decoupled from the flow, which means that their expected polarization degree is suppressed due to the ongoing scattering that is changing their Stokes parameters. Excluding $\theta_{\rm v} > 8°$ in the analysis of r_s in the *16TI* simulation changes it to be $r_s = 0.64$, which is consistent with the value acquired from the *40sp_down* simulation. Accompanying this feature is a switch in the polarization angle being consistent with 0° to then being consistent with 90°.

The time-integrated polarization is much smaller than what is found in other works. Ito et al. (2014) and Lundman et al. (2014) find Π as low as a few percent and as high as ~40%, for off-axis observers. The difference between our study and theirs can be attributed to the structure of the jet in the RHD simulation and the fact that not all photons are reaching the photosphere (typically located at $\gtrsim 10^{13}$ cm); this is shown in Figures 1 and 2. In Figure 3 we show the structure of the *16TI* and *40sp_down* jet as a function of angle at three different times in the jet's evolution, which correspond to various times in the synthetic light curves shown in the next section. The *16TI* simulation has a very fast core at all times. Initially, the jet is smaller than the wide jet presented by Lundman et al. (2014), but the *16TI* jet eventually grows to become larger, which has the effect of decreasing the amount of polarization. We additionally find that the *40sp_down* simulation has a relatively uniform Lorentz factor profile as a function of angle, although it does vary in time, which is expected from a variable jet. Both of these synthetic GRBs have very wide jets that contribute to the extremely low time-integrated polarization in Figure 2; these wide jets are relatively uniform and lacking steep gradients, a source of anisotropy in the flow, which means that there is little structure in the flow to produce very high time-integrated polarization (Lundman et al. 2014). Furthermore, the variability in the *40sp_down* simulation that should produce relatively large polarization ($\Pi \gtrsim 1\%$) gets washed out as we integrate over the bright and dim portions of the light curve and what is left is the effect of the very wide jet profile that we observe in Figure 3.

Although not all photons decouple from the jet, particularly at large $\theta_{\rm v}$ ($\gtrsim 9°$), there is still enough of an anisotropy in the outflow to produce polarization that is significantly different from $\Pi \approx 0\%$. Since the anisotropies in the outflow will only increase as the jet becomes increasingly transparent to the radiation, the polarization is expected to increase. Thus, we consider all of the polarization measurements at large $\theta_{\rm v}$ in our results to be lower limits.

3.2. Time-resolved Polarization

An advantage of using MCRaT on a time-dependent synthetic 2D RHD GRB jet is the ability to produce time-resolved polarization predictions. Figure 4 shows the time-resolved polarizations of the *16TI* simulation and the *40sp_down* simulations at two different observer angles. In the top panel we plot the light curves in black. In the bottom panel we show the

[4] The r_s values acquired are not statistically significant but they still provide a measure of how well correlated the variables are with respect to one another.

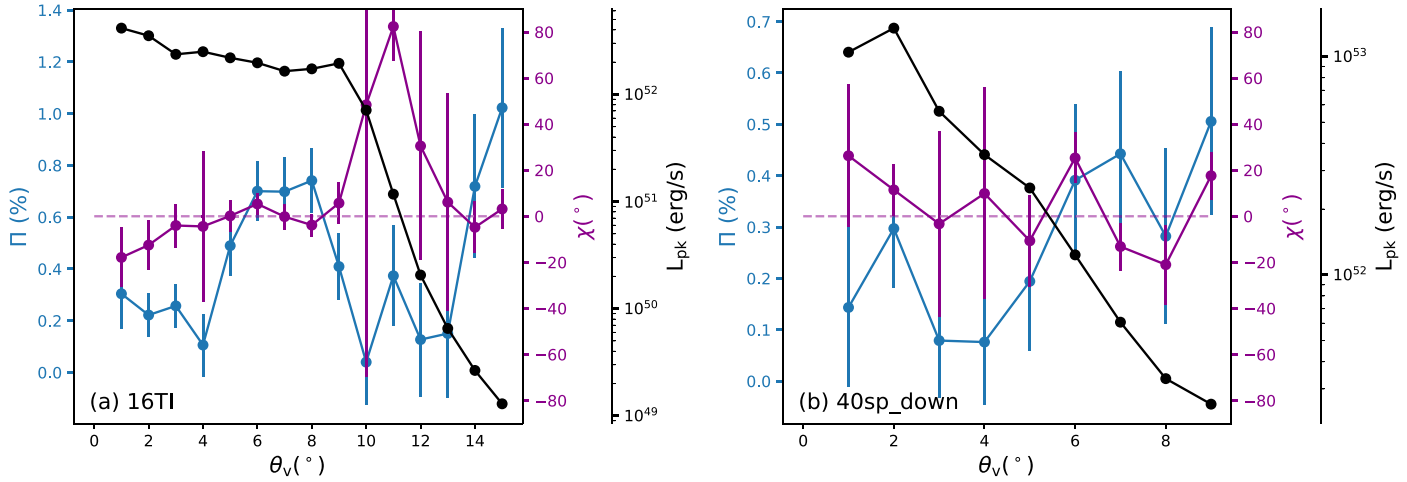

Figure 2. Time-integrated polarization degrees, plotted in blue, alongside the polarization angle, plotted in purple, and the peak luminosity of the light curve, plotted in black, at a given viewing angle, θ_v. The horizontal dashed line provides a reference for $\chi = 0°$. The left plot is for the *16TI* simulation and the right is for the *40sp_down* simulation. We find that the time-integrated Π in both simulations is inversely proportional to L_{pk} of the synthetic GRB. Similar to Figure 1, both figures shows a distinct decrease in Π in the *16TI* simulation around $\theta_v = 8°$ which is due to the fact that the photons at these larger viewing angles are not fully decoupled from the flow.

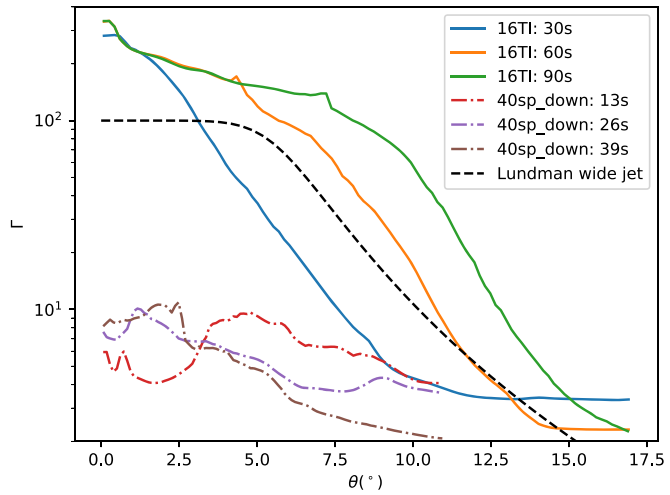

Figure 3. Plot of the Lorentz factor, Γ, of the synthetic *16TI* and *40sp_down* GRB jets as a function of angle at various times in its development. The times are associated with times that photons are detected in a given mock observed light curve. We also plot the Γ profile of the wide jet as given by Lundman et al. (2014) with $\theta_j = 0.1$ and $\Gamma_0 = 100$. The *16TI* simulation is initially more compact than Lundman et al.'s (2014) jet but evolved to be wider, decreasing the detected Π. The *40sp_down* simulation has a jet profile that is much wider than the wide jet in Lundman et al. (2014).

time-resolved polarization degree in black and the time-resolved polarization angle in purple. The dotted purple line is the $\chi = 0°$ reference line. The *16TI* simulation is binned uniformly in time with $dt = 0.5$ s and the *40sp_down* results are binned nonuniformly with a binning criteria based on the total energy received in each time bin. This energy must be larger than some critical luminosity before the end of the time bin is determined. Figures 4(b) and (c) have luminosity cutoffs of 2×10^{52} erg s^{-1} and 2×10^{51} erg s^{-1}, respectively.

For the case of the *16TI* GRB simulation, shown in Figure 4(a), the polarization is very small at all times ($\Pi \lesssim 1.5\%$). This can be attributed to the lack of structure in the jet, as is shown in Figure 3. The brighter portion of the light curve is indicative of low optical depth regions of the outflow (Parsotan et al. 2018); it is during this period that we get the most well-constrained polarization measurements (see Section 2.1 where the errors are $\propto N^{-\frac{1}{2}}$). We see that Π is also at its maximum, at $\sim$2%, and $\chi \approx 0°$ at all times during the maximum of the light curve. The *16TI* simulation does not have multiple shells of material coming into view of the observer's LOS. As a result, we can use it as a control for analyzing the *40sp_down* simulation.

Things are much different in the case of *40sp_down*, where the jet is variable and there is lots of time-dependent spatial structure on the scale of $\delta\theta \sim \Gamma^{-1}$, where Γ is $\sim$10 (see Figure 3). At $\theta_v = 2°$, in Figure 4(b), we see that Π is relatively small with a maximum of $\sim$2%. At this viewing angle we are in the core of the jet where the profile is relatively symmetric and, as a result, do not have much interference with off-axis shells of material coming into the observer's LOS. This case is very similar to the *16TI* simulation analyzed in Figure 4(a).

Figure 4(c) shows the *40sp_down* light curve, E_{pk}, Π, and χ for an observer at $\theta_v = 7°$. In this case, we observe larger Π, with the maximum being $\sim$5%. Additionally, the polarization angle changes multiple times during this synthetic GRB observation. On order to emphasize this oscillation in χ, we replot the largest pulse in Figure 4(c) using larger time bins of $dt = 0.5$ s in Figure 4(d). We see that within the first few seconds of the GRB, χ changes from 90° to 0° and back to 90° within a $\delta t \sim 1$ s. Then, $\chi \approx 0°$ during the brightest portion of the light curve, at $t \approx 13$ s. The constant value of χ is similar to what we see for the *16TI* simulation where there is little structure in the jet and we are seeing the main emission region along the observer's LOS. On the other hand, the changing χ suggests that other shells of material within the jet are coming into the observer's LOS due to variability in the jet.

In order to confirm that a changing χ is representative of various regions of the jet coming to the observer's LOS, we relate the times in the light curve shown in Figure 4(d) to equal arrival time surfaces within the jet. In Figure 5 we plot the density in a region of the jet that corresponds to the regions that are emitting during the times of interest in the light curve. These equal time of arrival surfaces are shown as a variety of different colored highlighted regions that correspond to the vertical highlighted regions plotted in Figure 4(d). We find that at $t = 11.0$–11.5 s the dense jet core ($\rho \sim 10^{-6}$ g cm^{-3} at

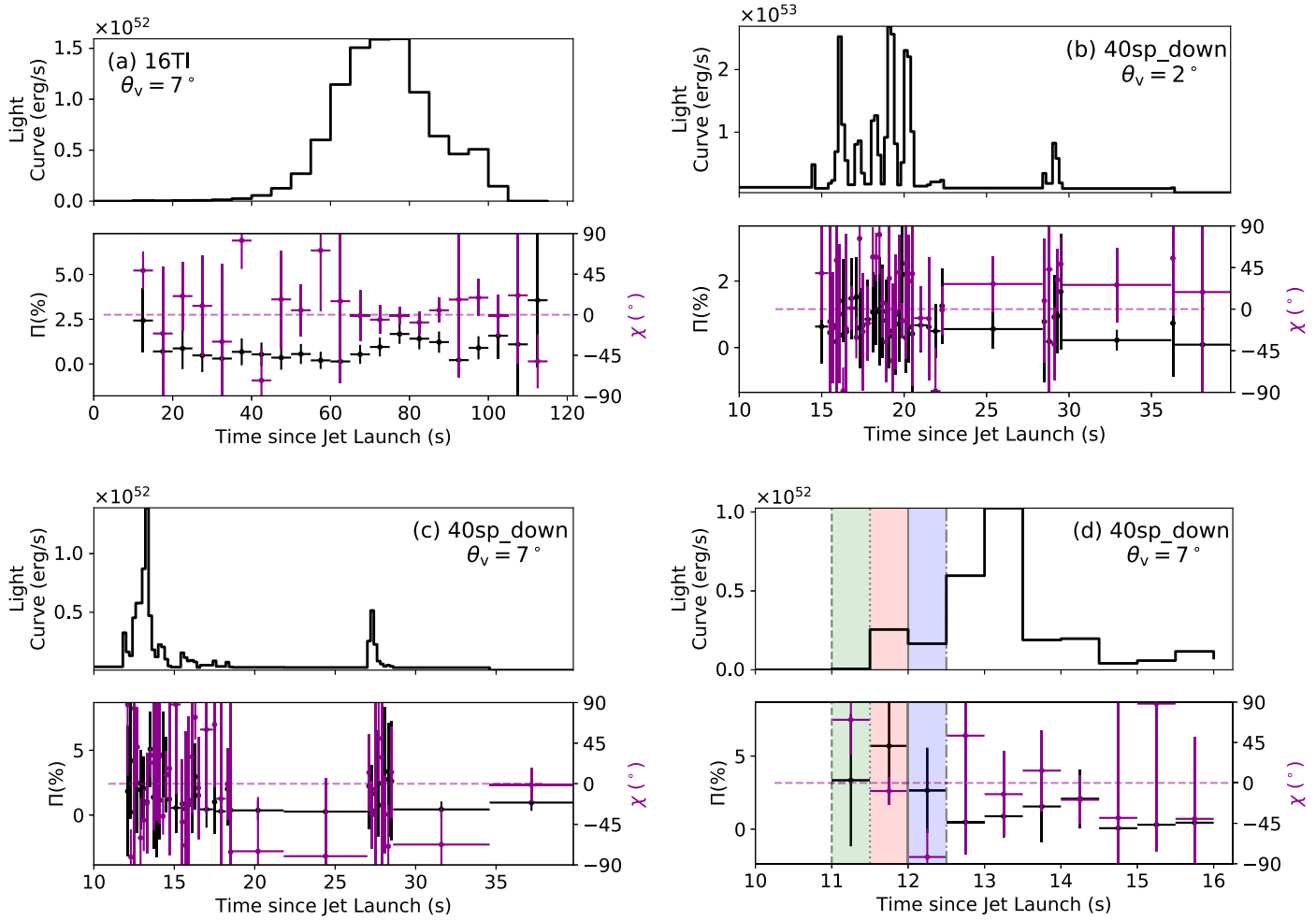

Figure 4. Light curves, polarization degrees, in black in the bottom panel, and polarization angles, in purple, for the *16TI* simulation, (a), and the *40sp_down* simulation for an observer located at 2° and 7°, (b) and (c), respectively. Panel (d) shows (c) with a larger time bin of 0.5 s. The horizontal dashed line in the bottom panels provides a reference for $\chi = 0°$. The highlighted green, red, and blue portions in (d), and the gray vertical lines, correspond to regions of equal arrival times shown in Figure 5 with similar lines. The *16TI* simulation does not exhibit much polarization while the polarization angle stays around 0° during the brightest portion of the light curve. The *40sp_down* simulation shows a relatively high polarization degree at larger viewing angles in addition to evolution of χ within the synthetic GRB ((d) at $t \sim 11.5$ s). We find that a changing χ is indicative of various shells of material coming into the LOS of the observer due to structure within the jet, while a constant χ indicates that the emission region is staying relatively constant due to lack of structures within the jet.

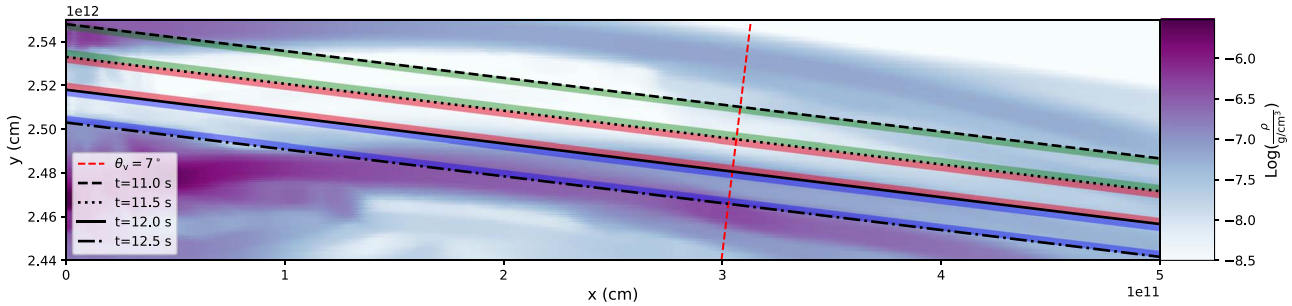

Figure 5. A pseudocolor density plot of a region of the *40sp_down* GRB simulation. The red dotted line corresponds to the line of sight of an observer located at $\theta_v = 7°$. The various lines are surfaces of equal arrival times that are detected by an observer at $\theta_v = 7°$ at various times. The highlighted regions, colored green, red, and blue, correspond to the start and end of the same colored regions shown in Figure 4(d). We find that the change in χ seen in Figure 4(d) is due to seeing different portions of the jet at various times. Initially, at $t = 11$ s, the observer sees the core of the jet. Then they observe photons originating from outer regions of the jet at $t = 11.5$–12 s. Finally, the observer sees more of the inner region of the jet again by $t = 12.5$ s.

$y \sim 2.54 \times 10^{12}$ cm and $x \sim 0$ cm) is the dominating emission material, scattering photons into the observer's LOS (Parsotan et al. 2018) with $\chi \approx 90°$. At $t = 11.5$–12 s, the emitting region is between two dense shells in the jet and the observed photons are primarily originating from the denser outer region of the jet, where $\rho \sim 10^{-7.5}$ g cm^{-3} located at $y \sim 2.47 \times 10^{12}$ cm and $x \sim 5 \times 10^{11}$ cm, changing χ to be $\approx 0°$. Finally, by $t = 12.5$ s, the observer sees emission from the inner region of the jet again, near $x \sim 2 \times 10^{11}$ cm and $y \sim 2.48 \times 10^{12}$ cm where $\rho \sim 10^{-6.5}$ g cm^{-3}, thus changing the polarization angle once more. The width between the two dense shells of material corresponds to the $c\delta t$ of the changing χ. The outlined effect of a

changing χ as related to the lateral and temporal structure of the jet is seen by an observer located at $\theta_v = 3°$–$8°$. The upper limit is related to the fact that photons are not fully decoupled from the flow at $\theta_v \gtrsim 9°$ and the lower limit is due to the core of the jet being the dominating emission region at all times for $\theta_v \lesssim 3°$.

The changing χ that we observe are consistent with the observed changing polarization angle of GRB 170114A (Zhang et al. 2019). These changing χ from the *40sp_down* simulation also suggest that the jet that produced GRB 170114A was variable.

4. Summary and Discussion

We have used the MCRaT code to conduct Monte Carlo radiation transfer simulations of time-resolved and time-integrated polarization in LGRBs. MCRaT injects, propagates, and Compton scatters photons using the full KN cross section. These photons are injected into an outflow described by a FLASH 2D RHD simulation and are subsequently scattered until the end of the simulation. This process of injecting, propagating, and scattering photons is repeated until there are no more photons to be injected in the simulation. The implementation of polarization in MCRaT was verified in multiple ways and we were able to recover the time-integrated polarization profile of a wide jet as presented by Lundman et al. (2014). We ran the MCRaT simulations using the RHD simulations of a steady GRB jet, the *16TI* simulation, and a variable engine jet, which we denote as the *40sp_down* simulation.

Primarily, we have found that:

1. Not all photons at large θ_v ($\gtrsim 9°$) in the MCRaT simulation are decoupled from the synthetic GRB jet which decreases the mock observed Π; as a result, the Π presented in this paper at large θ_v are lower limits.
2. The time-integrated polarizations are generally positively correlated with θ_v, with $r_s \approx 0.65$ for both simulations, and negatively correlated with L_{pk}, with the correlation between Π and L_{pk} being $r_s = -0.6$ and $r_s = -0.27$ for the *16TI* and *40sp_down* simulations, respectively.
3. The *16TI* simulation has very little structure on the scale of Γ^{-1} which decreases Π and contributes to χ being approximately constant in time.
4. The *40sp_down* simulation shows more structure temporally and spatially which contributes to various shells of materials coming into the LOS of the observer, as a result, this simulation has larger time-resolved $\Pi \sim 5\%$ and a changing χ.
5. The δt for χ to change in a variable jet is indicative of the width of shells of materials within the GRB jet.
6. A changing χ also indicates that the observer is seeing various regions of the GRB jet, which may help constrain temporal and lateral variability in the jet structure.

The MCRaT results of the time-integrated quantities ($\Pi \lesssim 1\%$ and $\chi \approx 0°$) are consistent with the results presented by Lundman et al. (2014), where wider jets produce lower polarization degrees, however our results show the importance of ensuring that all photons are decoupled from the flow. Our simulations have a finite domain which prevents some photons at $\theta_v \gtrsim 9°$ from being decoupled from the flow by the time they propagate to the edge of the simulation domain. As Parsotan et al. (2018) mentioned, the peaks in the light curves are composed of photons that are mostly decoupled from the outflow while the quiescent portions are still coupled to the flow. The dimmer regions contribute to lowering the overall time-integrated Π, although we do detect some polarization from these dimmer times in the light curves due to structure in the GRB outflow (Lundman et al. 2014). As the photons become less coupled to the outflow, the asymmetry in the jet will become more pronounced with respect to the radiation and we will expect to detect larger Π. This drives the need to conduct larger domain RHD simulations, to ensure that the photons at larger θ_v ($\gtrsim 9°$) are decoupled from the flow and we have an accurate mock observation of Π at these large angles.

The results presented here are consistent with the results found by Zhang et al. (2019). Our mock detected Π are within the limits that they find for their GRBs ($\Pi \lesssim 10\%$). In particular, Zhang et al. (2019) provide a 99th percentile upper limit of $\Pi < 28\%$ for GRB 170114A, but quote $\Pi \approx 4\%$ which is consistent with the Π that we acquire in our study.

Additionally, we are able to show that variable GRB jets can produce changing χ such as is observed in GRB 170114A. Zhang et al. (2019) report the χ of the aforementioned GRB to be 122° for the first portion of the burst and 17° for the second portion. While our polarization angles can only change between 0° and 90° due to the symmetry of the simulations, we may see a continuous change in χ from 3D MCRaT simulations. Additionally, Zhang et al. (2019) do not specify any errors on their values of χ in GRB 170114A, however, their plots of the fitted Π and χ parameters' confidence contours show that χ is not well constrained. As a result, it is still possible that χ is $\sim 0°$ or $\sim \pm 90°$ which is expected for an axis-symmetric jet, such as the ones studied in this work. The fact that the *40sp_down* simulation produces a changing χ suggests that GRB 170114A had a variable jet, with various parts of the jet coming into the observer's line of sight. Our results are also able to explain the changing χ seen by Sharma et al. (2020) for GRB 160821A.

One important assumption that Zhang et al. (2019) make is that Π is constant throughout a GRB and χ can change in time. In our analysis we find that this assumption may not be valid (see for example Figure 4(d) where both Π and χ change). Even if the GRB has a steady jet being injected (which is not known a priori), χ will be approximately constant and Π may change (see Figure 4(a)).

With future GRB polarimetry missions, such as POLAR-2 (Kole 2019) and LEAP (McConnell et al. 2017), expected to observe GRB polarizations with higher precision than that of the POLAR detector, we can use our findings to place constraints on the expected Π and χ of the photospheric model compared to other GRB emission models. Globally, we expect the polarization angle, χ, to be $\sim 0°$ or $\sim 90°$. While it is possible that the photospheric model may be able to account for other values of χ in 3D, it is unlikely that the polarization angle will deviate significantly from being aligned perpendicular or parallel to the plane defined by the jet axis and the observer's LOS. Thus, a measurement of χ that is significantly different from these values combined with a large value of Π may indicate that there is a global magnetic field in the jet (Toma et al. 2009). In the case of a random magnetic field, the observed Π will be low and the observed value of χ would be $\sim 0°$ (Toma et al. 2009; Gill et al. 2019), similar to the photospheric case. The ability of the photospheric model to account for very low and high values of time-integrated

polarization degrees based on the geometry of the jet (Lundman et al. 2014) makes it very difficult to distinguish from the synchrotron model, with a global or random magnetic field, based solely on that observed parameter. As a result, time-resolved Π and χ observations become much more important. The results acquired in this work suggests that GRBs observed on axis will have small $\Pi \lesssim 2\%$ and constant χ, during the brightest portion of the light curve, while GRBs observed off-axis will have larger Π and χ that change by $\sim 90^{\circ}$ with the temporal structure of the GRB. If the emission mechanism is synchrotron with a global magnetic field, the Π and χ should not change in time; however with a random magnetic field, Π and χ may vary randomly based on the magnetic field configuration of the GRB at a given time at a given observer LOS (Gill et al. 2019). There still needs to be more research conducted to produce robust time-resolved polarization degree and angle predictions for a variety of jet structures and magnetic field configurations, for each emission model.

Unlike the analysis conducted by Lundman et al. (2018), we do not consider the polarization at various energy bands. Lundman et al. (2018) has shown that this can be an interesting area of testing the photospheric model and the capability of testing time-resolved polarization of different energy bands can also prove to be fruitful. With this goal in mind, and to ensure that there are enough low energy photons in the outflow (Parsotan & Lazzati 2018; Parsotan et al. 2018), MCRaT will be modified to consider the effects of synchrotron radiation and absorption. This improvement, combined with larger domain RHD simulations will allow us to make stringent time-integrated and time-resolved predictions of GRB spectra and polarizations.

We would like to thank Hirotaka Ito, Christoffer Lundman, and Henric Krawczynski for discussion about the Stokes parameters and ways to ensure that MCRaT properly accounts for the Stokes parameters in every frame of reference. We thank them for sharing their codes with us.

T.P. and D.L. acknowledge support by NASA grants 80NSSC18K1729 (Fermi) and NNX17AK42G (ATP), Chandra grant TM9-20002X, and NSF grant AST-1907955. T.P. acknowledges funding from the Future Investigators in NASA Earth and Space Science and Technology (FINESST) Fellowship, NASA grant 80NSSC19K1610. Resources supporting this work were provided by the NASA High-End Computing (HEC) Program through the NASA Advanced Supercomputing (NAS) Division at Ames Research Center. Additionally, this work used the CoSINe High Performance Computing cluster, which is supported by the College of Science at Oregon State University. D.L.C. is supported by Cátedras CONACyT at the Instituto de Astronomía (UNAM) and acknowledges the support from the Miztli-UNAM supercomputer (project LANCAD-UNAM-DGTIC-321).

Appendix
Comparing MCRaT to Other Analyses

To show that the cross section sampling algorithm and Lorentz boosting of the Stokes parameters are correct, we reproduce some results acquired by Depaola (2003) and Krawczynski (2011).

Figure A1 shows the resulting modulation curve when our KN cross section is Monte Carlo sampled in black. The analytic profile of the cross section as a function of $\phi_{\rm sc}$ calculated by Depaola (2003) is shown as the solid blue line. They sample the KN cross section for a photon beam with 100% polarization along the $+Q$ direction, with an energy of 100 keV and $85^{\circ} < \theta_{\rm sc} < 90^{\circ}$. Accounting for the differences in the positive Stokes parameters in the convention used, we are able to use our method of sampling the Stokes parameter to acquire the proper distribution.

In order to verify the algorithm of switching frames of reference, we reproduce the results acquired by Krawczynski (2011). Krawczynski (2011) scattered a beam of photons, 100% polarized along the $+Q$ axis with frequency $\omega = 10^{12}$ Hz, with a beam of electrons moving at a Lorentz factor of $\gamma = 100$. Following their setup, we produce distributions of the resulting lab frame stokes parameters as a function of scattering angles, which we show in Figure A2. These distributions are identical, with the exception of normalization, to the distribution acquired by Krawczynski (2011) in their Figure 6. The difference in the signs of Q and U in our distribution with respect to Krawczynski's (2011) Figure 6 is due to the differences in the orientation of the $+Q$ and $+U$ axis of the Stokes plane.

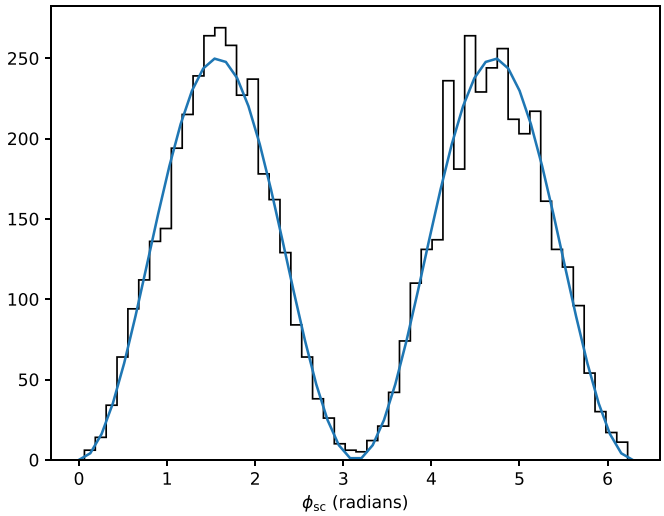

Figure A1. Plot of the distributed $\phi_{\rm sc}$ from sampling the KN cross section as is outlined in Section 2.2 compared to the analytic cross section acquired by Depaola (2003). The distribution is shown in black and the analytic profile is shown by the blue curve.

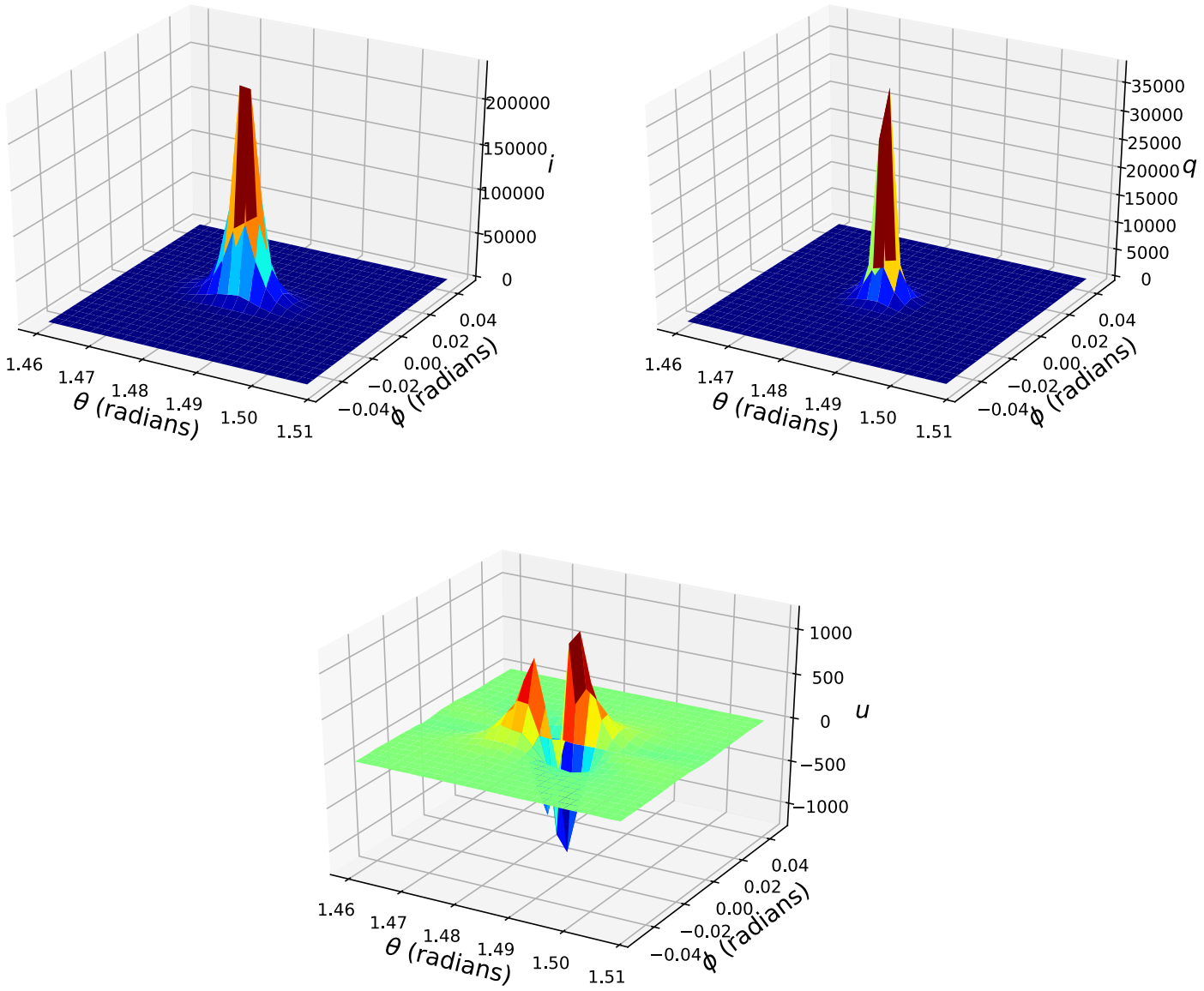

Figure A2. The distribution of the Stokes parameters as a function of the scattered photon's θ and ϕ values. These distributions are morphologically similar to the distribution acquired by Krawczynski (2011) in thier Figure 6.

ORCID iDs

Tyler Parsotan https://orcid.org/0000-0002-4299-2517
Diego López-Cámara https://orcid.org/0000-0001-9512-4177
Davide Lazzati https://orcid.org/0000-0002-9190-662X

References

Abbott, B. P., Abbott, R., Abbott, T. D., et al. 2017, ApJL, 848, L13
Amati, L., Frontera, F., Tavani, M., et al. 2002, A&A, 390, 81
Beloborodov, A. M. 2010, MNRAS, 407, 1033
Beloborodov, A. M. 2011, ApJ, 737, 68
Bloom, J. S., Kulkarni, S. R., Djorgovski, S. G., et al. 1999, Natur, 401, 453
Burgess, J., Kole, M., Berlato, F., et al. 2019, A&A, 627, A105
Chhotray, A., & Lazzati, D. 2015, ApJ, 802, 132
Deng, W., & Zhang, B. 2014, ApJ, 785, 112
Deng, W., Zhang, H., Zhang, B., & Li, H. 2016, ApJL, 821, L12
Depaola, G. 2003, NIMPA, 512, 619
Gill, R., Granot, J., & Kumar, P. 2019, MNRAS, 491, 3343
Goldstein, A., Veres, P., Burns, E., et al. 2017, ApJL, 848, L14
Golenetskii, S. V., Mazets, E. P., Aptekar, R. L., & Ilyinskii, V. N. 1983, Natur, 306, 451
Hjorth, J., Sollerman, J., Møller, P., et al. 2003, Natur, 423, 847
Ito, H., Matsumoto, J., & Nagataki, S. 2019, NatCo, 10, 504
Ito, H., Matsumoto, J., Nagataki, S., Warren, D. C., & Barkov, M. V. 2015, ApJL, 814, L29
Ito, H., Nagataki, S., Matsumoto, J., et al. 2014, ApJ, 789, 159
Kalemci, E., Boggs, S. E., Kouveliotou, C., Finger, M., & Baring, M. G. 2007, ApJS, 169, 75
Kislat, F., Clark, B., Beilicke, M., & Krawczynski, H. 2015, APh, 68, 45
Klebesadel, R. W., Strong, I. B., & Olson, R. A. 1973, ApJL, 182, L85
Kole, M. 2019, ICRC (Madison), 36, 572
Krawczynski, H. 2011, ApJ, 744, 30
Lan, M.-X., & Dai, Z.-G. 2020, ApJ, 892, 141
Lazzati, D. 2016, ApJ, 829, 76
Lazzati, D., Morsony, B. J., & Begelman, M. C. 2009, ApJL, 700, L47
Lazzati, D., Morsony, B. J., Margutti, R., & Begelman, M. C. 2013, ApJ, 765, 103
Lazzati, D., Perna, R., Morsony, B. J., et al. 2018, PhRvL, 120, 241103
López-Cámara, D., Morsony, B. J., & Lazzati, D. 2014, MNRAS, 442, 2202
Lundman, C., Pe'er, A., & Ryde, F. 2014, MNRAS, 440, 3292
Lundman, C., Vurm, I., & Beloborodov, A. M. 2018, ApJ, 856, 145
Lyutikov, M., Pariev, V., & Blandford, R. D. 2003, ApJ, 597, 998
MacFadyen, A. I., Woosley, S. E., & Heger, A. 2001, ApJ, 550, 410
Mathews, K. 2013, NSE, 173, 207
McConnell, M. L., Baring, M. G., Bloser, P. F., et al. 2017, HEAD, 16, 103.20

McMaster, W. H. 1961, RvMP, 33, 8
Mochkovitch, R., & Nava, L. 2015, A&A, 577, A31
Parsotan, T., & Lazzati, D. 2018, ApJ, 853, 8
Parsotan, T., López-Cámara, D., & Lazzati, D. 2018, ApJ, 869, 103
Pe'er, A. 2008, ApJ, 682, 463
Pe'er, A., Mészáros, P., & Rees, M. J. 2006, ApJ, 642, 995
Pe'er, A., & Ryde, F. 2011, ApJ, 732, 49
Produit, N., Bao, T., Batsch, T., et al. 2018, NIMPA, 877, 259
Rees, M. J., & Mészáros, P. 1994, ApJL, 430, L93
Rees, M. J., & Mészáros, P. 2005, ApJ, 628, 847
Rybicki, G. B., & Lightman, A. P. 1979, Radiative Processes in Astrophysics (New York: Wiley-Interscience)
Sharma, V., Iyyani, S., & Bhattacharya, D. 2020, MNRAS, 493, 5218
Toma, K., Sakamoto, T., Zhang, B., et al. 2009, ApJ, 698, 1042
Waxman, E. 2003, Natur, 423, 388
Woosley, S. E., & Heger, A. 2006, ApJ, 637, 914
Yonetoku, D., Murakami, T., Gunji, S., et al. 2011, ApJL, 743, L30
Yonetoku, D., Murakami, T., Nakamura, T., et al. 2004, ApJ, 609, 935
Zhang, B., & Yan, H. 2010, ApJ, 726, 90
Zhang, S.-N., Kole, M., Bao, T.-W., et al. 2019, NatAs, 3, 258